ADVANCED MATERIALS
www.advmat.de

Composite Spin Hall Conductivity from Non-Collinear Antiferromagnetic Order

Steve Novakov, Peter B. Meisenheimer, Grace A. Pan, Patrick Kezer, Nguyen M. Vu, Alexander J. Grutter, Ryan F. Need, Julia A. Mundy, and John T. Heron**

Non-collinear antiferromagnets (AFMs) are an exciting new platform for studying intrinsic spin Hall effects (SHEs), phenomena that arise from the materials' band structure, Berry phase curvature, and linear response to an external electric field. In contrast to conventional SHE materials, symmetry analysis of non-collinear antiferromagnets does not forbid non-zero longitudinal and out-of-plane spin currents with $\hat{x}, \hat{z}$ polarization and predicts an anisotropy with current orientation to the magnetic lattice. Here, multi-component out-of-plane spin Hall conductivities σ_{xz}^{x}, σ_{xz}^{y}, σ_{xz}^{z} are reported in $L1_2$-ordered antiferromagnetic $PtMn_3$ thin films that are uniquely generated in the non-collinear state. The maximum spin torque efficiencies ($\xi = J_S/J_e \approx 0.3$) are significantly larger than in Pt ($\xi \approx 0.1$). Additionally, the spin Hall conductivities in the non-collinear state exhibit the predicted orientation-dependent anisotropy, opening the possibility for new devices with selectable spin polarization. This work demonstrates symmetry control through the magnetic lattice as a pathway to tailored functionality in magnetoelectronic systems.

1. Introduction

Thin film antiferromagnets have emerged as strong candidates for state-of-the-art spintronic applications, promising efficient spin current generation that is critical for the development of low power non-volatile electronics.[1,2,3] Currently, intrinsic spin current generation in thin films has relied on non-magnetic materials, originating from interfacial symmetry breaking[4,5] (such as the Rashba–Edelstein effect), crystalline symmetry breaking,[6,7,8] surface spin current from a topological insulator state,[9,10,11] or a bulk spin Hall effect from high band spin-orbit coupling in materials such as W or Pt.[12,13,14,15] In bulk SHE systems, the Berry phase curvature originates from spin-orbit coupling and is maximal when the spin-orbit splitting between bands is small and the Fermi level is between the opened gap, maximizing the contribution to the linear response tensor.[12,15,16] In systems with highly magnetic atomic species, additional Berry curvature can arise from itinerant electron interaction with the magnetic lattice (*s-d* model), a mechanism that predicts large intrinsic spin conductivities without any contribution from spin-orbit coupling.[17,18] Furthermore, the reduced symmetry of non-collinear magnetic lattices, compared to non-magnets or ferromagnets, allows for unconventional non-zero components of the

S. Novakov
Department of Physics
University of Michigan
Ann Arbor, MI 48109, USA
E-mail: steveeee@umich.edu

P. B. Meisenheimer, N. M. Vu, J. T. Heron
Department of Material Science and Engineering
University of Michigan
Ann Arbor, MI 48109, USA
E-mail: jtheron@umich.edu

G. A. Pan, J. A. Mundy
Department of Physics
Harvard University
Cambridge, MA 02138, USA

P. Kezer
Department of Electrical and Computer Engineering
University of Michigan
Ann Arbor, MI 48109, USA

A. J. Grutter, R. F. Need
NIST Center for Neutron Research
National Institute of Standards and Technology
Gaithersburg, MD 20899-6102, USA

R. F. Need
Department of Materials Science and Engineering
University of Florida
Gainesville, FL 32611, USA

The ORCID identification number(s) for the author(s) of this article can be found under https://doi.org/10.1002/adma.202209866

DOI: 10.1002/adma.202209866

linear response tensors for charge and spin currents. For instance, breaking twofold rotational symmetry or inversion permits out-of-plane spin currents with additional $\hat{x}$, $\hat{z}$ polarization and intrinsic longitudinal spin currents.[19,20,21] Detailed theoretical work computing the intrinsic spin Hall conductivities in the XMn_3 (X = Rh, Ir, Pt) materials shows highly anisotropic spin conductivity and large non-zero amplitudes for unconventional polarizations.[22] Compared to high symmetry non-magnetic materials with high spin-orbit coupling (e.g., fcc Pt, Laue group $m\bar{3}m1'$), which have spin Hall conductivity tensor components restricted to that of the canonical spin Hall effect (e.g., only $\sigma^{y}_{xz}, -\sigma^{z}_{xy}$ contributions for an applied current along $\hat{x}$), the reduced symmetry of the cubic $PtMn_3$ non-collinear state (Laue group $\bar{3}m'1$) allows for additional transverse and also longitudinal spin conductivity for multiple spin polarizations.[19] Furthermore, the conductivities can be anisotropic with respect to current orientation, potentially allowing for selection of preferred spin current direction and polarization.[22,23] Recent work with the non-collinear $IrMn_3$ system yielded a large facet-dependent spin Hall conductivity,[23] though it showed only conventional σ^{y}_{xz}, and it was not directly linked to the AFM order due to the large Néel temperature ($T_N \approx 1000$ K).[24] In Mn_3Sn, the direction of the order parameter (the magnetic octupole moment of a noncollinear spin lattice) has been shown to create large σ^{z}_{xz}, and that its relative amplitude to σ^{y}_{xz} can be tuned by changing this orientation.[25] The near room temperature accessibility of three distinct magnetic textures (non-collinear, collinear, and non-magnetic)[26,27] makes $PtMn_3$ a uniquely suitable material for studying intrinsic AHE/SHE that originates from electron exchange with the magnetic lattice. For the AHE, a link with the antiferromagnetic order has been presently established, using both temperature and piezoelectric strain to move a $PtMn_3$ film out of the non-collinear AFM state and suppress the intrinsic AHE entirely.[28] In our work, we have synthesized $L1_2$ ordered (001)-oriented $PtMn_3$ thin films in isolation and in heterostructures with Permalloy (Py, here approximately $Ni_{80}Fe_{20}$) to measure the anomalous (σ_{xy}) and out-of-plane spin Hall conductivities (σ^{i}_{xz}, $i \in (x, y, z)$) in each of the accessible antiferromagnetic phases with second harmonic Hall effect measurements and to explicitly correlate them with magnetic order and show the expected anisotropy in the spin Hall conductivity. We observe that the maximum spin torque efficiencies ($\xi = J_S / J_e \approx 0.3$) from the unconventional $\hat{x}, \hat{z}$ polarized out-of-plane spin currents are significantly larger than the traditional $\hat{y}$ polarized out-of-plane spin current in Pt ($\xi \approx 0.1$). This orientation-dependent anisotropy and high efficiency is promising for efficient switching of magnetic devices and devices with selectable spin polarization components.

2. Results and Discussion

Thin film $PtMn_3$ samples in this study were grown on (001)-oriented $SrTiO_3$ substrates via RF magnetron sputtering (see Experimental Section). A representative X-ray diffraction (XRD) $2\theta - \omega$ scan of a 95 nm $PtMn_3$ film on $SrTiO_3$, as well as a ϕ scan of the substrate and $PtMn_3$ 024 peaks, is shown in **Figure 1**b. The $PtMn_3$ films are predominantly (001)-oriented, with thicker films showing detectable amounts of (111) oriented domains (though these are consistently < 1% of the total film volume). The $L1_2$ ordering fraction of the $PtMn_3$ film in Figure 1b, calculated from the ratio of the 001 and 002 integrated peak intensities (see Experimental Section), is 0.91, with the rest of the film assumed to be the solid solution γ-$PtMn_3$. High-angle annular dark field scanning transmission electron microscopy (HAADF-STEM) images of the same 95 nm $PtMn_3$ film is shown in Figure 1c. Over the imaged region, the films are single crystal, (001)-oriented, and $L1_2$ ordered, although occasional antisite defects are observed. Unpolarized neutron reflectivity measurements (see Experimental Section) reveal a transition region near the substrate with different stoichiometry to the bulk (see Note S1, Supporting Information, for a detailed discussion). The resulting scattering length density (SLD) profiles yield a Pt-rich transitional growth region of 18.4 ± 0.3 nm (unless otherwise noted, all uncertainties represent ±1 standard deviation) with an approximate stoichiometry of $PtMn_{2.0}$, followed by a uniform "bulk-like" layer of near optimal stoichiometry, approximately $PtMn_{2.7}$ (see SLD profile in Figure S2, Supporting Information). We anticipate this transition region exists due to the large lattice mismatch (≈1.8% in-plane lattice mismatch between (001)-oriented $SrTiO_3$ and bulk cubic $PtMn_3$), which favors the γ phase with reduced manganese stoichiometry to relax the epitaxial strain. For our transport studies, the existence of this transition region necessitates $PtMn_3$ films thicker than 20 nm for harmonic Hall effect measurements. Independent of this transition region, deposition conditions were tuned to target a slight Mn deficiency ($x = -0.07$ for $Pt_{1-x}Mn_{3+x}$) in order to reduce transition temperatures below 400 K to make them more accessible for electrical measurements.[26] X-ray photoelectron spectroscopy (XPS) measurements of the Mn 2*p* and Pt 4*f* peaks (see Experimental Section) yield a stoichiometry of approximately $PtMn_{2.77\pm 0.07}$ ($x = -0.06 \pm 0.02$ for $Pt_{1-x}Mn_{3+x}$) near the surface of the film, within the desired range, and in agreement with the neutron reflectivity data.

Electrical measurements of $PtMn_3$, Py, and $PtMn_3$/Py films were performed on Hall devices with 10 μm × 40 μm channels for longitudinal and Hall resistivity measurements (see Experimental Section for fabrication details). The general measurement scheme and angular coordinate system for harmonic Hall effect measurements is shown in Figure 1d. Zero field R_{xy} versus temperature of $SrTiO_3$/$PtMn_3$(95 nm) films is shown in Figure 1e. There is a clear intermediate phase between 150 and 200 K where the films have significant remnant magnetization in the out-of-plane direction that does not saturate for maximum fields up to 9 T. As shown in Figure 1f, an increase in the zero-field Hall resistance emerges smoothly below T_N and undergoes a first-order transition between 200 and 300 K, after which it diminishes. The temperature difference between the first-order and Néel transition is ≈150 K, and the overall profile matches that of the neutron diffraction intensity of the half-order ($10\frac{1}{2}$) peaks in prior studies of bulk $PtMn_3$ with stoichiometry that closely matches that of our films.[26] These peaks correspond well to the emergence of an intermediate collinear AFM state, which has a magnetic lattice symmetry between the high temperature non-magnetic metal and the low temperature non-collinear AFM. With respect to the bulk material, the transition temperatures in the $SrTiO_3$/$PtMn_3$ samples are shifted downward from 50 to 100 K, which we attribute to a combination of tetragonal strain from the substrate lattice mismatch (c/a ≈ 0.98 at 300 K) and

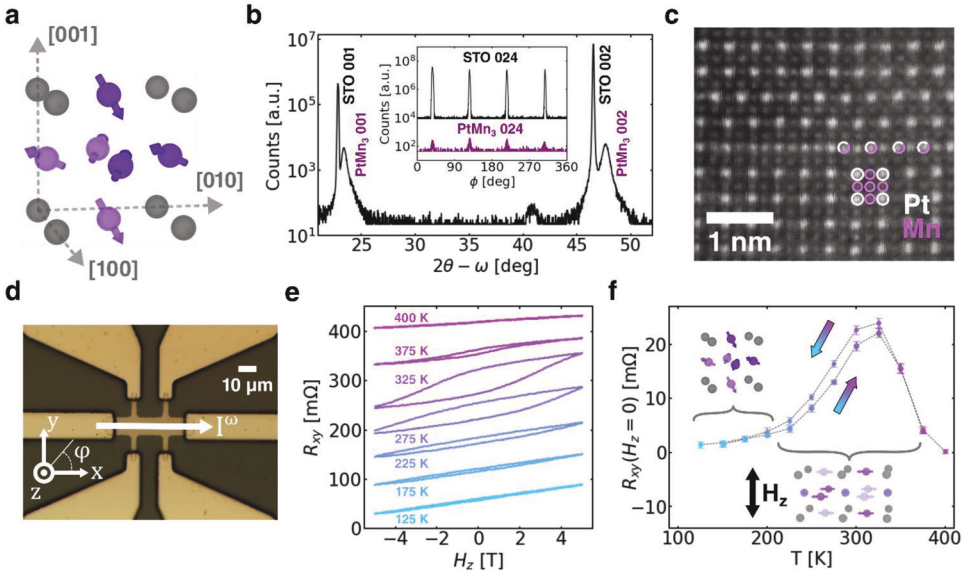

Figure 1. Structural properties and magnetic phase transitions of $PtMn_3$ thin films on (001)-oriented $SrTiO_3$. a) The low temperature non-collinear AFM state of $L1_2$ ordered $PtMn_3$ with Pt on the vertices (gray) and Mn on the face sites (purple). b) XRD of 001 $PtMn_3$ on $SrTiO_3$ (STO) with ϕ scan (inset). c) STEM micrograph of representative $PtMn_3$ thin film showing Pt (white), Mn (purple), and occasional Mn/Pt substitutional defects (white/purple). Thin films on $SrTiO_3$ used in this study exhibit $L1_2$ ordering fractions of 0.70–0.91 with thinner films typically having higher ordering. d) Schematic of longitudinal and transverse measurement coordinates for patterned $PtMn_3$ and $PtMn_3$/Py Hall devices. e) Anomalous Hall resistance of $SrTiO_3/PtMn_3$ (95 nm) versus out-of-plane field H_z and temperature T (offset for clarity). f) Remnant zero-field anomalous Hall resistance from 5 T training field versus temperature of $SrTiO_3/PtMn_3$ (95 nm) (error bars represent 2 standard deviations of R_{xy} for H_z up to ±500 Oe at each temperature in (b). The intermediate state of large R_{xy} ($H_z = 0$) corresponds well to a high susceptibility state with remnant ferromagnetic canting in the out-of-plane direction from field cooling (inset). The observed first order transition between 250–300 K is consistent with bulk $PtMn_3$, but shifted lower in temperature by 50–100 K.

reduced Mn stoichiometry. This stoichiometric influence on transition temperature and lattice constant has been previously studied in detail,[26] and recent work has shown that even slight differences in deposition rate can cause a large shift.[29] In attempting to directly probe these phase transitions with neutron diffraction of $SrTiO_3/PtMn_3$(95 nm) samples, we found that it was not possible to resolve distinct $PtMn_3$ peaks due to the significant overlap with the substrate. Instead, we performed temperature dependent diffraction studies on films grown on MgO, which confirms a ≈400 K Néel transition, though films on MgO are significantly less ordered and exhibit higher epitaxial strain (see Note S2 and Figure S3, Supporting Information). Polarized neutron reflectometry shows that $MgO/PtMn_3$ films are exclusively antiferromagnetic and have no net moment (see Figure S1, Supporting Information). As the Néel and first-order transition are now electrically accessible, we measure the spin conductivity in each explicit regime and link its structure directly to the AFM order.

We evaluate the spin current being injected into the Py layer by the $PtMn_3$ with harmonic Hall measurements, whereby a harmonic current is applied to the bilayer that induces spin canting in the ferromagnet layer, which is encoded in the second harmonic magnetoresistance.[30,31,32] Under an injected spin current with polarization $\hat{p}$, the magnetization dynamics in the ferromagnet layer are described by the Landau–Lifshitz–Gilbert–Slonczewski (LLGS) equation: $\dot{\hat{m}} = -\gamma \hat{m} \times H_{\text{eff}} + \alpha \hat{m} \times \dot{\hat{m}} + \gamma H_{\parallel} \hat{m} \times \hat{p} \times \hat{m} + \gamma H_{\perp} \hat{p} \times \hat{m}$, where H_{eff} encapsulates crystal and shape anisotropy fields, as well as any external fields H_{ext}, and $H_{\parallel}$ and $H_{\perp}$ are the damping-like and field-like spin torque effective fields, respectively. Here, the notation $H_{\parallel} = H_{\text{DL}}$ and $H_{\perp} = H_{\text{FL}} - H_{\text{Oe}}$ is adopted to separate the damping-like and field-like contributions from spin transfer torques from that of the Oersted field from an applied total current in adjacent film layers or interfaces. These magnetization dynamics are coupled to the magnetoresistance through the anomalous and planar Hall effects: $R_{xy}(\theta, \varphi) = R_A \cos\theta + R_P \sin^2\theta \sin 2\varphi$, where the magnetization orientation is $\hat{m} = \cos\varphi \sin\theta \hat{x} + \sin\varphi \sin\theta \hat{y} + \cos\theta \hat{z}$, with $\hat{z} \parallel [001]$ for our thin film samples. When a current is applied to the heterostructure, the spin currents generated in the $PtMn_3$ layer diffuse upward into the Py and deflect the magnetization away from its equilibrium orientation by some small $\Delta\theta$, $\Delta\varphi$ depending on the strength of $H_{\parallel}$, $H_{\perp}$. To claim that the origin of these perturbations is the intrinsic spin current from the antiferromagnet and rule out anomalous self-torques, the Py film must have a smooth interface, be not much thicker than 4 nm, and the anisotropy must be that of an ideal uniaxial in-plane ferromagnet.[33] The spin transfer interface of the $SrTiO_3/PtMn_3$(46.6 nm)/Py(6.8 nm)/SiC sample used for harmonic Hall measurements is shown in a STEM micrograph in **Figure 2**a. There is no significant roughness or atomic mixing between the $PtMn_3$ and Py films, and the interfacial transition length is conservatively bounded at 1 nm. This thickness was deemed to be optimal due to the ≈20 nm transition region from the substrate (see Figure S2, Supporting Information) and corresponds to the approximate minimal thickness that the lattice constant approaches the bulk value with thinner films

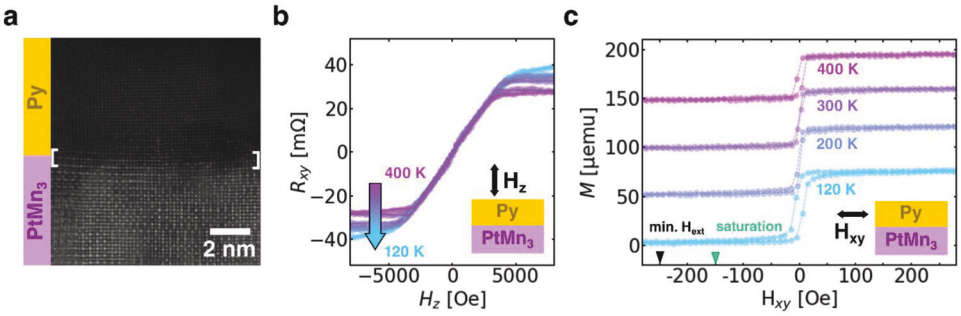

Figure 2. Interface quality and magnetic anisotropy of $PtMn_3$/Py. a) STEM micrograph of the $PtMn_3$/Py interface of the $SrTiO_3$/$PtMn_3$ (46.6 nm)/Py(6.8 nm)/SiC sample used for harmonic Hall measurements showing high crystalline ordering and an interface transition region <1 nm. The smoothness and quality of the spin Hall/ferromagnet interface reduces anomalous spin torques and ensures the maximal intrinsic response. b) Out-of-plane field anomalous Hall effect scans of patterned $SrTiO_3$/$PtMn_3$ (46.6 nm)/Py(6.8 nm)/SiC Hall devices from 120–400 K, showing smooth linear behavior in the low field regime across the full temperature range. c) In-plane VSM of a 5 mm × 3 mm piece of the same $SrTiO_3$/$PtMn_3$ (46.6 nm)/Py(6.8 nm)/SiC sample used for Hall devices from 120–400 K and up to ±250 Oe under an applied 50 Oe training field during temperature sweeps. Note that 1 emu = 1 mA m^2. At all temperatures, there is no significant exchange bias and the Py is well saturated in-plane at 250 Oe, the minimum used for second harmonic Hall effect measurements, ensuring monodomain-like behavior for the spin transfer torque measurements.

showing high tetragonal strain.[29] From out of plane anomalous Hall effect field sweeps (Figure 2b) and in-plane vibrating sample magnetometry (Figure 2c), the Py in our $PtMn_3$/Py bilayers has the ideal in-plane uniaxial anisotropy and is totally saturated in-plane at ≈150 Oe for all temperatures between 120 and 400 K. For the in-plane harmonic Hall effect study, the minimum field used is 250 Oe, and the Py is expected to behave as a ferromagnetic monodomain. A general schematic for the bilayer harmonic Hall effect measurement in this regime is shown in **Figure 3**a.

Spin currents in the non-collinear phase of $PtMn_3$ are predicted to be anisotropic and carry unconventional transverse polarization due to itinerant carrier exchange with the low-symmetry Kagome lattice.[18,22,23] Charge current applied in the high symmetry [111] direction leads to only a conventional spin Hall-like texture, while charge currents in the Kagome plane lead to transverse spin currents that have spin polarizations $\hat{p} \parallel$ [111] (see schematic in Figure S7, Supporting Information).[23] The film plane in our samples is (001) and not the high symmetry (111) orientation, so we expect a linear combination of these two modes depending on in-plane orientation. We probe this orientation-dependent anisotropy of spin Hall conductivity by orienting Hall devices along the [100], [110], [010], and [$\bar{1}$10] crystal axes. The expected anisotropy can be determined from the symmetry transformations of spin Hall conductivity tensors $\bar{\sigma}^i$, $i \in (x, y, z)$ as done previously[22] and projected into the coordinate system of our Hall devices. For a spin Hall conductivity tensor with polarization component p' in some global basis, the expected spin current in a Hall device with channel orientation $\hat{E}$ (parallel to the in-plane longitudinal electric field) is $J^{p}_{E,r} = \sum_{p'}(\hat{p}\cdot\hat{p}')[\mathbf{R}\cdot\sigma^{p'}\cdot\mathbf{E}]$, where $\mathbf{R} = \sum_{p'}(\hat{r}\cdot\hat{p}')\hat{p}'$, $\mathbf{E} = \sum_{p}(\hat{E}\cdot\hat{p}')\hat{p}'$ are the projections of the spin current direction and applied electric field into the original basis. These calculations are explained in detail in Note S5 (Supporting Information). The theoretically expected spin conductivities for a device with a single (111)-oriented antiferromagnetic domain are shown in Figure 3b. In general, the σ^i_{xz} components are highly anisotropic with respect to the crystal orientation, and each component has a respective set of orientations where it dominates. This analysis explains results from a parallel work, in which substrate epitaxy was used to orient the magnetic lattice of the noncollinear state.[34] Surprisingly, this work did not report any σ^x_{xz} spin torques, though they are expected for any devices that strongly project to [100]-equivalent orientations. We speculate that some difference between measurement schemes (spin torque ferromagnetic resonance (STFMR) versus harmonic Hal effect) hides these components, though they were resolved in Mn_3GaN with the same method.[21] In the most general case here, a single global AFM domain will generate some combination of $\hat{p} = \hat{x}, \hat{y}, \hat{z}$, polarized spin current. Assuming some contribution from all possible polarization components, the expected in-plane second harmonic response is:

$$V^{2\omega}_{xy} = V' \sin 2\varphi + CR_0 I_a^2 \cos\varphi + \frac{1}{2}\frac{R_A I_{FM} J_{SHM}}{H_{ext}+H_S}\left(h^x_{DL}\sin\varphi - h^y_{DL}\cos\varphi + h^z_{FL}\right) + \frac{R_P I_{FM} J_{SHM}}{H_{ext}}\cos 2\varphi\left(h^x_{FL}\sin\varphi - \left(h^y_{FL} - h_{Oe}\right)\cos\varphi + h^z_{DL}\right) \quad (1)$$

where $H^i_{FL,\,DL} = J_{SHM}\, h^i_{FL,DL}$ for $i \in (x,\ y, z)$ are the components of spin current polarization, and the second term, $CR_0 I^2_{total}\cos\varphi$ is a separate contribution from the anomalous Nernst effect, which arises from out-of-plane thermal gradients present in every thin film system.[31] In our cryogenic system (see Experimental Section), we find a non-field-dependent $V'\sin 2\varphi$ term emerges below 150–200 K, which we speculate is some small injection of the driving harmonic signal through the external wiring that becomes measurable at lower temperatures. V' in all devices measured here is typically <500 nV or approximately < 5% of the $V^{2\omega}_{xy}$ amplitude at 120 K and does not vary with field. We adopt a current-density based convention for the damping like (h^i_{DL}) and field-like (h^i_{FL}) spin torque effective fields in Oe per

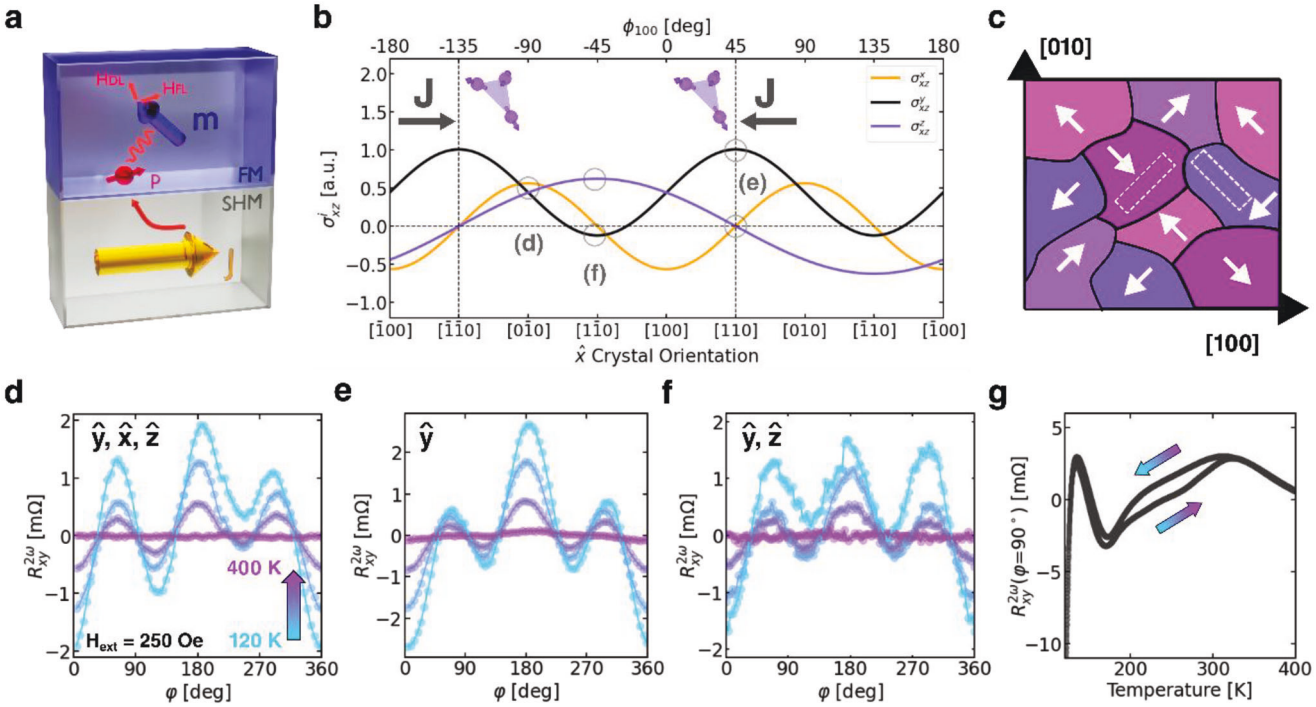

Figure 3. Current and domain orientation versus spin torque components in $PtMn_3$/Py. a) Simplified schematic of out-of-plane spin current from σ^i_{xz} $i \in (x, y, z)$ generated in the AFM spin Hall material with net polarization $\hat{p}$ diffusing into a ferromagnetic layer and causing field-like and damping-like spin torques. b) Current orientation dependence of σ^i_{xz} for a device with a single (111)-oriented antiferromagnetic domain, and with a Hall device $\hat{x}$ oriented at an in-plane angle ϕ from the [100] crystal direction using $\bar{\sigma}^i$ from Ref. [22] and transforming into the device coordinates. c) Schematic of possible non-collinear AFM domain orientation in (001) plane (white arrows are in-plane [111] projections), and degeneracy with two Hall bars oriented orthogonally to the crystal lattice but with identical magnetic lattices. Second harmonic Hall resistance at $H_{ext} = 250$ Oe for temperatures between 120–400 K for devices with significant d) σ^x_{xz}, e) σ^y_{xz}, f) σ^x_{xz} which emerge below 200 K. In (d), (e), and (f) some low temperature curves (e.g., those with high $\hat{z}$ signature) are vertically centered for a clear symmetry comparison. g) A clear first-order transition is seen in the in-plane $R^{2\omega}_{xy}$ at in-plane angle $\varphi = 90°$ that matches that seen in the anomalous Hall resistance. Unlike with conventional $\hat{p} = \hat{y}$, $R^{2\omega}_{xy}$ varies significantly with T, H_{ext} at $\varphi = 90°$, $270°$ when $\hat{p} = \hat{x}, \hat{z}$ components are present. Aligning devices to a preferred AFM texture orientation is difficult due to AFM domain formation as highlighted in (c) though it is possible to find devices with dominant $\hat{p} = \hat{x}, \hat{y}, \hat{z}$ components.

10^7 A cm^{-2} (1 Oe = 79.6 A m^{-1}), which is normalized for the current density in the $PtMn_3$ film layer. We note that only the $PtMn_3$ film within ≈10 nm of the Py interface is likely to be relevant to the harmonic Hall effect measurements due to the low spin diffusion length in metals, typically 1–10 nm.[35] For our harmonic Hall effect measurements, we grew heterostructures of $SrTiO_3$/$PtMn_3$(46.6 nm)/Py(6.8 nm)/SiC, keeping Py below ≈10 nm thickness to minimize any anomalous second harmonic response from out-of-plane spin texture formation in the Py layer.[33] In general, the $PtMn_3$/Py interface is smooth, showing less than 1 nm peak-to-peak-roughness, though we observe occasional pockets of cubic Mn at the surface, attributed to manganese diffusion at elevated temperatures (see Note S3, Figures S4 and S5, Supporting Information). To quantify the current distribution in bilayer $PtMn_3$/Py devices, 4-wire resistivity measurements were performed on isolated films and a parallel resistor model was used to estimate the current splitting (see Note S4, Supporting Information).

In addition to current orientation, it is critical to consider the size and orientation of antiferromagnetic domains. Below the first-order transition, the Kagome planes of the low-temperature $PtMn_3$ phase could be oriented in any (± 1 ± 1 ± 1) equivalent direction. If a Hall device is rotated 90° in-plane with respect to the crystal lattice, but the AFM lattice is also rotated accordingly, then there is no change to the system from re-orienting the device, as outlined in Figure 3c. As shown in Figure S8 (Supporting Information), the presence of unconventional $\hat{x}$, $\hat{z}$ components is only expected in configurations with low global symmetry, with the high-symmetry limit of totally random domain orientation reducing to a conventional $\hat{y}$-only spin Hall effect system, despite the existence of the noncollinear state in each domain (Figure S8g, Supporting Information). In general, field-training non-collinear antiferromagnetic domains are not a well-defined practice, and we rely on sampling multiple devices of the same crystal orientation. Additionally, the size of AFM domains in thin films can range from 10 s of nm to several μm,[36,37,38] and it is plausible that our 10 μm wide Hall devices can contain multiple domains. In general, multiple AFM domains in equivalent proportion serve to reduce the orientation dependent anisotropy of the σ^i_{xz}, and in the case of having all possible domains equally present, quench them entirely (see Note S5 and Figure S8, Supporting Information). Despite the difficulties in orienting the non-collinear AFM lattice, we observe second harmonic Hall data that yield a clear contribution from σ^x_{xz}, σ^y_{xz}, and σ^z_{xz}, respectively, in Figure 3d–

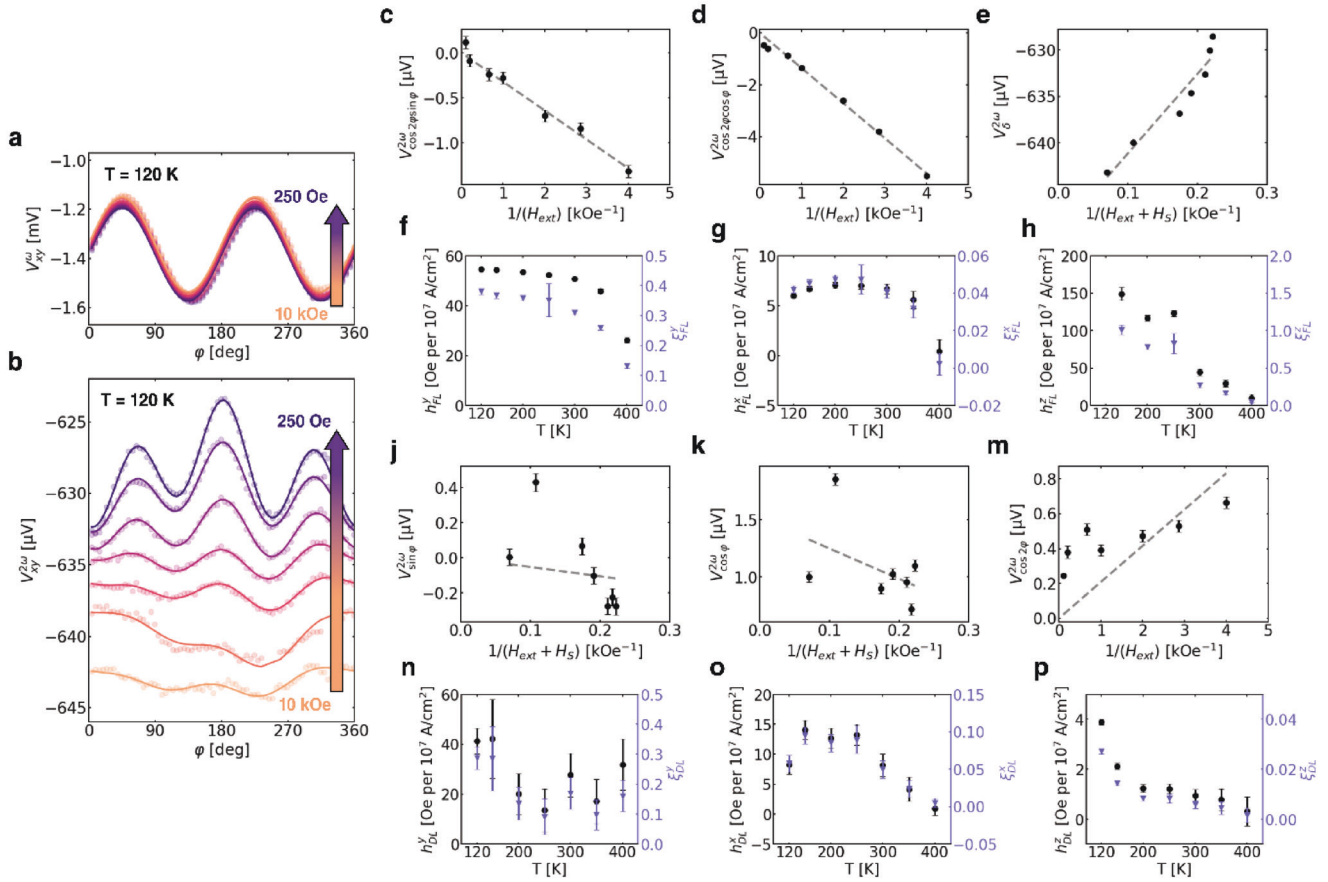

Figure 4. Second harmonic Hall effect and spin torque effective fields versus temperature in a $PtMn_3$/Py Hall device with $\hat{x}$, $\hat{y}$, $\hat{z}$ spin torques. Representative φ, H_{ext} scans of a) first and b) second harmonic Hall resistance of a $PtMn_3$ (46.6 nm)/Py(6.8 nm) device with visible effects of unconventional σ^x_{xz}, σ^z_{xz}. c–e) A breakdown of field-like spin torque components at 120 K by symmetry as a function of $1/H_{ext}$ and $1/(H_{ext} + H_S)$, and f–h) the resulting spin torque effective fields h^i_{FL} versus temperature. j–m) The same inverse field dependence of the damping-like spin torque components at 120 K, and n–p) the resulting spin torque effective fields versus temperature (error bars represent 2 standard deviations as reported by the DREAM parameter estimation). It is difficult to extract the damping-like components with high precision when all three field types are present due to their small relative signal-to-noise (≈2% of the entire signal per component). The torques from the $\hat{x}$, $\hat{z}$ polarized spin currents are only significant below 200–250 K, commensurate with the emergence of the noncollinear $PtMn_3$ AFM phase.

f. These unconventional profiles emerge at temperatures below 200 K, below the observed first-order transition in the zero-field AHE data in Figure 1f and suggest that these devices are mostly a single AFM domain. Whenever there is a dominant σ^i_{xz} component, it is possible to visually identify it from the second harmonic data due to the unique symmetry in φ for each spin torque effective field contribution to $R^{2\omega}_{xy}$ (see Note S6 and Figure S9, Supporting Information). Compared to the expected $R^{2\omega}_{xy}$ from only σ^y_{xz}, the unconventional σ^x_{xz}, σ^y_{xz} cause significant and nonzero field-dependent variation around $\varphi = 90°, 270°$, as shown in Figure S9b–e (Supporting Information). To explicitly link the emergence of σ^x_{xz}, σ^z_{xz} with the magnetic transitions shown with neutron diffraction and temperature dependent anomalous Hall effect measurements, we measure $R^{2\omega}_{xy}(\varphi = 90°)$ with a slow and continuous temperature sweep between 400 and 120 K, shown in Figure 3g. We note a clear first order transition between 200 and 300 K, commensurate with the out-of-plane anomalous Hall effect data in Figure 1f. This points to the noncollinear ordering of the low temperature phase as the clear origin of these unconventional components.

The field and in-plane angle dependence of a representative first and second harmonic scan is shown in **Figure 4**a,b for a $SrTiO_3$/$PtMn_3$(46.6 nm)/Py(6.8 nm)/SiC Hall device oriented in a (100)-equivalent direction at 120 K. The first harmonic profile does not change significantly with H_{ext} and follows the expected sin 2φ profile with no change in amplitude, which indicates good saturation of the Py layer for all H_{ext} and good thermalization. The corresponding second harmonic profiles are drastically different from the typical spin Hall effect result, which has dominant cos 2φcos φ and cos φ components. Here, the dominant spin conductivity is σ^z_{xz} and there is a strong field-dependent cos 2φ and vertical offset instead. The dependence of each separate $R^{2\omega}_{xy}$ component versus $1/H_{ext}$ (for in-plane deflections) and $1/(H_{ext} + H_S)$ (for out-of-plane deflections) is shown in Figure 4c–e for field-like components and Figure 4j–m for damping-like components for the same device at 120 K. The extracted

spin torque effective fields and corresponding spin transfer torque efficiencies $\xi_{STT} = J_S/J_e = \frac{1}{J_e}\left(\frac{2e}{\hbar}\right) M_S t_{FM} H_{DL}$ are shown in Figure 4f–h for field-like components and Figure 4n–p for damping-like components over the full temperature range of 120–400 K. In general, the components that scale like $1/H_{ext}$ can be accurately extracted and conform to the expected inverse field relation. This property is held across the full temperature range as shown in Figure S11 (Supporting Information). In contrast, the $1/(H_{ext} + H_S)$ components, which are over 10 times smaller in signal amplitude for low H_{ext}, are difficult to accurately extract when all three components are present, and the resulting effective field calculation yields large errors, up to 50%. All components follow the expected field relations well except for the vertical offset component corresponding to h_{FL}^{z}, which is much larger than expected and has a large offset at high fields. For devices with field-dependent offsets and cos 2φ components, we calculate h_{FL}^{z} up to ≈1400 Oe per 10^7 A cm^{-2} in some devices at 120 K, but cannot fully justify this value due to the relatively smaller h_{FL}^{y} (<100 Oe per 10^7 A cm^{-2} for all devices) and the fact that the theoretical calculations predict approximately the same maximum amplitude for $\sigma_{xz}^{y}, \sigma_{xz}^{z}$ (see Figure 3b). In Figure 4h, we report the extracted h_{FL}^{z}, up to ≈150 Oe per 10^7 A cm^{-2}, but are unsure whether it can be solely attributed to interfacial spin accumulation. We discuss some potential origins of this offset behavior in Note S6 (Supporting Information). We speculate that the interactions across a ferromagnet–antiferromagnet interface may complicate the established second harmonic Hall effect model. Though we establish no significant exchange bias in the $PtMn_3$/Py bilayers in the antiferromagnetic $PtMn_3$ phases (Figure 2b,c), transport experiments may be more sensitive to small volumes of anomalous spin texture near the interface that do not significantly impact wide-area measurements such as VSM. We speculate that further magnetic decoupling of the Py from the $PtMn_3$ with a thin nonmagnetic spacer layer (e.g., Cu) may reduce this anomalous response and lead to improved spin transfer.[39]

The field-like and damping-like spin torque effective fields are shown for all devices in this study as a function of temperature in Figure S10 (Supporting Information). The effective fields from the spin Hall conductivities σ_{xz}^{x} and σ_{xz}^{z} emerge suddenly below 200–250 K and are near zero at higher temperatures, corresponding well to the phase transitions seen in the anomalous Hall conductivity profile in Figure 1e,f, corroborated with the explicit first-order phase transition in $R_{xy}^{2\omega}$ as shown in Figure 3g. As per the symmetry analysis in Figure S9 (Supporting Information), $R_{xy}^{2\omega}$ at $\varphi = 90$ is uniquely sensitive to $\hat{x}, \hat{z}$ polarization components and not to $\hat{y}$ components that clearly link the first-order transition in $R_{xy}^{2\omega}$, the non-collinear phase of $PtMn_3$ and the unconventional $\hat{x}, \hat{z}$ components of the spin Hall conductivity. At 120 K, devices with significant σ_{xz}^{z} yield $h_{DL}^{z} = 3.5 \pm 1.6$ Oe per 10^7 A cm^{-2}, and devices with significant σ_{xz}^{x} contributions yield $h_{DL}^{x} = 53 \pm 31$ Oe per 10^7 A cm^{-2}. In the large σ_{xz}^{x} and σ_{xz}^{z} devices at 120 K, $\xi_{STT}^{x} = 0.37 \pm 0.22$ and $\xi_{STT}^{z} = 0.02 \pm 0.01$. Overall, these spin torque efficiencies are comparable to typical ξ_{STT}^{y} reported for intrinsic SHE in single heavy element thin films[12,16,35] despite the 75% reduction in Pt content and are attributed to the itinerant exchange physics from the antiferromagnetic order. Unlike the corresponding $\hat{p} = \hat{x}, \hat{z}$ components, h_{FL}^{y} follows the profile of a typical Néel transition, rising monotonically below 400 K, though there is a slight bifurcation between devices below 200 K that we attribute to the onset of the intrinsic and orientation-dependent σ_{xz}^{y} from the non-collinear state, the polarity of which can vary with AFM lattice orientation. While there are no expected σ_{xz}^{x}, σ_{xz}^{z} from the collinear AFM state, the symmetry does not prevent an intrinsic isotropic σ_{xz}^{y},[18,19,40] and the additional change from the onset of the non-collinear phase is <10% of the intermediate phase value. In contrast to other recent observations of $\hat{p} = \hat{x}, \hat{z}$ spin currents in non-collinear AFMs,[21,41] our samples yield higher average h_{DL}^{x}/h_{FL}^{y} (≈ 0.81) and similar h_{DL}^{z}/h_{FL}^{y} (≈ 0.06) and are highly anisotropic with respect to crystal/AFM domain orientation. The notion that these components are exclusively tied to exchange physics in the non-collinear state is well supported by their lack of existence in the collinear and nonmagnetic states above 200–250 K. This corresponds well with a recent study of Mn_3GaN, which has no intermediate collinear state, and where these components emerge smoothly through the Néel transition.[21] It is also possible that the intrinsic efficiency is higher than reported due to the likelihood of randomly oriented domain nucleation during cooling, as illustrated in Figure 3c, with the effect of reducing the unconventional $\hat{x}, \hat{z}$ torques (see Figure S8, Supporting Information). If domain nucleation can be controlled to guarantee a single global noncollinear domain or if a different system can be discovered with higher selectivity, it may be possible to extract the effective fields with more precision.

3. Conclusion

To summarize, thin film $PtMn_3$ with high $L1_2$ ordering generates unconventional spin Hall conductivity tensor components (σ_{xz}^{x}, σ_{xz}^{z}) that have an orientation-dependent anisotropy, are unique to the non-collinear AFM state, and are consistent with symmetry analysis. This current direction-dependent anisotropy can be used to change the ratio of $\hat{p} = \hat{x}, \hat{y}, \hat{z}$ out-of-plane spin current and select for a dominant polarization component. The mean spin transfer torque efficiencies in our $PtMn_3$ devices ($\xi_{DL}^{x} = 0.37$, $\xi_{DL}^{z} = 0.04$, $\xi_{DL}^{y} = 0.46$) match or exceed that of the canonical fcc Pt, which supports itinerant electron exchange with the magnetic lattice as a stronger mechanism for spin current generation than spin-orbit coupling.[18] Our results suggest that noncollinear antiferromagnets could bridge the gap in spin torque efficiency between heavy metals such as Pt, W, and topological insulators such as 2D bismuth selenides[11] and tellurides.[42] Moreover, the strong orientation-dependent anisotropy of the spin Hall conductivity offers selectivity of out-of-plane spin current polarization, which may enable new developments in low power nonvolatile spin-based electronics.

4. Experimental Section

Film Growth: The $PtMn_3$ films were grown via RF magnetron sputtering from a 1″ metallic target of 6:1 Mn:Pt at 45 W, 650 °C substrate temperature, 5″ target-substrate distance, and in 10 mTorr (1 mTorr = 0.133 Pa) of Ar at ≈1.5 nm min^{-1}. For growths on MgO, the substrate was pre-baked at 950 °C for 1 h in vacuum. For growths on $SrTiO_3$, the substrate was pre-baked at 650 °C for 30 min in 50 mTorr Ar. After deposition, films were either cooled to room temperature immediately at 15 K min^{-1} in 50 mTorr Ar or annealed at 700 °C for 1 h in 50 mTorr Ar. Permalloy

films were deposited at room temperature from a 2″ target of $Ni_{80}Fe_{20}$ at 100 W, approximately 5″ target-substrate distance, and in 10 mTorr of Ar at ≈2.5 nm min^{-1}. For capping with SiC or Ti, the sample was removed from the chamber and placed in a high vacuum pulsed laser deposition chamber within 1 min of sample removal for capping film deposition.

X-Ray Diffraction: The structure was characterized by X-ray diffraction (XRD) in a Rigaku SmartLab diffractometer equipped with a Ge(220) × 2 monochromator to select for Cu Kα. XRD φ scans were obtained by aligning to 024 peaks of the substrates and film. Reciprocal space mapping was done by aligning to the substrate 024 peaks and scanning in 2θ, ω in ≈3° fields of view and 0.1° resolution. To quantify the ordering fraction, the relative intensity of the out-of-plane 001 and 002 $PtMn_3$ XRD peaks is compared to the ideal crystal with 100% ordering. To extract the intensities, Voigt profiles are fit to the substrate and $PtMn_3$ XRD peaks. For the 001, 002 XRD peaks, $I_{001}/I_{002} = S^2\ r_0$, where S is the ordering fraction, and $r_0 = 0.938$ is the ratio for the fully ordered crystal. In all samples used in this study, $S_{STO} \in [0.7,\ 0.91]$, with thinner films typically exhibits higher ordering fractions.

X-Ray Photoelectron Spectroscopy: XPS spectra were obtained using a Kratos Axis Ultra XPS with a monochromated Al source and a charge neutralizer. High-resolution scans were taken at the Mn 2p and Pt 4f peaks. The integrated intensities of the Mn 2p 1/2 and Pt 4f 5/2 peaks were compared to those from a reference 6:1 Mn:Pt target to establish film stoichiometry.

Neutron Diffraction: Neutron diffraction measurements of $MgO/PtMn_3$(150 nm)/Py (9 nm)/TiO_2 (6 nm) films were taken in the SPINS, BT4 and BT7 instruments at the NIST Center for Neutron Research. On SPINS the incident and scattered neutron energy was 5 meV (λ = 4.04 Å) selected by pyrolitic graphite (PG) monochromator and analyzer crystals with Be-filters before and after the sample position to eliminate higher-order neutrons. On BT4 and BT7, incident neutrons of 14.7 meV (λ = 2.359 Å) energy were selected, using PG filters to eliminate the higher-order neutrons. Measurements were carried out in a temperature range of 100–420 K in a closed-cycle refrigerator. Diffraction measurements of $SrTiO_3/PtMn_3$(95 nm)/SiC films were taken in the CANDOR white beam reflectometer/diffractometer at the NIST Center for Neutron Research. Measurements on CANDOR were performed with an incident white beam of neutrons with wavelengths ranging between 4 and 6 Å (2.2–5.1 meV). Wavelengths outside this band were removed using an upstream Be-filter and an X-reflector section of neutron guide. Individuate wavelength bands were separated from the scattered beam and directed into detectors using a series of 54 graphite monochromator crystals.

Neutron Reflectometry: Polarized and unpolarized neutron reflectometry measurements were performed using the PBR and CANDOR instruments, respectively, at the NIST Center for Neutron Research. The polarized measurements were performed on a $MgO/PtMn_3$ (150 nm)/Py (9 nm)/TiO_2 (6 nm) heterostructure at room temperature in an applied magnetic field of 3 T. Incident and scattered neutrons were spin-polarized parallel or antiparallel to the applied magnetic field, and the data were corrected for imperfect beam polarization and spin-flipper performance. The spin-dependent reflectivity was measured as a function of the momentum transfer vector Q along the film normal. Data were reduced using the Reductus software package, while nuclear SLD and magnetic SLD depth profiles were extracted by fitting the data with the Refl1D software package for reflectometry modeling.[43,44] Uncertainties in fitted parameters were extracted using the Differential Evolution Adaptive Metropolis (DREAM) method as implemented in the Bumps python package.[45]

Scanning Transmission Electron Microscopy: Cross-sectional samples for scanning transmission electron microscopy (STEM) were prepared with an FEI Helios 660 focused-ion beam (FIB) using standard liftout techniques. The final thinning process was performed using 2 keV Ga ions. Atomic-resolution HAADF-STEM imaging was performed with 200 keV electrons on an aberration-corrected JEOL ARM 200F with a probe convergence angle of ≈22 mrad, probe currents of ≈27 pA, and an ADF collection angle range of 68–220 mrad. Electron-energy loss spectroscopy (EELS) spectra (Note S3, Supporting Information) were recorded with a Gatan Enfinium ER (model 977) spectrometer with a probe current of ≈50 pA. All STEM images are presented as raw data with no filtering applied. EELS spectra were background subtracted using a linear combination of power laws and integrated over ≈10 eV across each edge.[46]

Sample Patterning: Thin film samples were patterned using conventional UV photolithography processes at the University of Michigan Lurie Nanofabrication Facility. Designs were written on 4″ fused silica mask plates using a Heidelberg DWL-2000 mask maker with a 4 mm write head. The photolithography for the ion milling and deposition patterns was done using a conventional SPR 220 based process. All samples were ion milled using an Intivac Nanoquest II Ar ion mill at a working temperature of 15 °C and an incident beam angle of 15°. The Ti(10 nm)/Pt(100 nm) metal contact layer was deposited on top of a deposition lithography mask via pulsed laser deposition (PLD) within a standard metal lift-off process.

Vibrating Sample Magnetometry: Vibrating sample magnetometry was performed on 5 mm × 3 mm samples in a Quantum Design Dynacool PPMS with the VSM option at temperatures between 120 and 400 K and with a 50 Oe cooling field. The sample was thermalized at each temperature step for 1 h.

Electrical Measurements: Electrical measurements at 10–150 °C were performed in a custom-built electronic transport rotator with χ and ϕ rotation capabilities and a Lakeshore EM4-HVA electromagnet. Measurements in the range of 20–400 K were performed in a Quantum Design Dynacool PPMS with the standard ETO puck, the horizontal rotator accessory option, and a custom breakout box for electronic instruments. First and second harmonic components were demodulated simultaneously using an Ametek DSP 7265 lock-in amplifier running in dual harmonic mode at a source frequency of 1937 or 2377 Hz. Thermal drift and the background anomalous Nernst effect signal are reduced by using $J_{PtMn_3} < 5 \times 10^6$ A cm^{-2} across the full temperature range. Samples were thermalized for 0.5–1 h with the standard ETO puck and up to 1.5 h on the horizontal rotator. Longitudinal and Hall resistances of patterned Hall devices were obtained via DC 4-point measurements with a Keithley 2450 sourcemeter. Uncertainties in fitted parameters were extracted using the Differential Evolution Adaptive Metropolis (DREAM)[45] method as implemented in the Bumps python package using 10^6–10^7 samples per fit.

Supporting Information

Supporting Information is available from the Wiley Online Library or from the author.

Acknowledgements

S.N., N.V., and J.T.H acknowledge support from the Semiconductor Research Corporation (SRC) as the NEWLIMITS Center and NIST through award number 70NANB17H041. P.B.M. and J.T.H. acknowledge support from The University of Michigan Rackham Predoctoral Fellowship. P.K and J.T.H acknowledge support from NSF MRSEC DMR-2011839. Electronic device fabrication was performed at the University of Michigan Lurie Nanofabrication Facility (LNF). G.A.P. acknowledges support from the Paul & Daisy Soros Fellowship for New Americans and from the NSF Graduate Research Fellowship grant no. DGE-1745303. J.A.M. acknowledges support from the Gordon and Betty Moore Foundation's EPiQS Initiative, Grant GBMF6760 and from the Packard Foundation. R.F.N. acknowledges support from the National Research Council Research Associateship Program. Facilities support was made through the National Science Foundation grant No. DMR-0420785 (XPS) and NSF major research instrumentation grant No. DMR-1428226 (PPMS). Electron microscopy was performed at Harvard University's Center for Nanoscale Systems (CNS), a member of the National Nanotechnology Coordinated Infrastructure Network (NNCI), supported by NSF grant no. 1541959. Access to CANDOR was provided by the Center for High Resolution Neutron Scattering, a partnership between the National Institute of Standards and Technology and the National Science Foundation under Agreement No. DMR-2010792. Certain trade names and company products are identified to specify adequately the experimental procedure. In no case does such identification

imply recommendation or endorsement by the National Institute of Standards and Technology nor does it imply that the products are necessarily the best for the purpose. This work was performed in part at the University of Michigan Lurie Nanofabrication Facility. The authors thank Dr. Guangyong Xu, Dr. Zhijun Xu, and Yang Zhao for assistance with the neutron diffraction measurement. The authors thank Ziji Xiang, Kuan-wen Chen, and Lu Chen for electronic experiment support.

Conflict of Interest

The authors declare no conflict of interest.

Author Contributions

S.N. grew thin films via magnetron sputtering deposition, fabricated devices, performed electrical, magnetic, and chemical characterization, and designed the transport experiments under the guidance of J.T.H. S.N and P.K. performed temperature-dependent harmonic Hall effect measurements. P.B.M. and S.N. performed structural characterization via XRD. N.V. grew thin films via pulsed laser deposition. A.J.G. and R.F.N performed structural and magnetic characterization via neutron diffractometry and polarized/unpolarized neutron reflectivity. G.A.P. performed STEM measurements under the guidance of J.A.M. S.N. prepared the manuscript with input from all authors.

Data Availability Statement

The data that support the findings of this study are available from the corresponding author upon reasonable request.

Keywords

antiferromagnets, low symmetry, spin Hall effect, spin torques, thin films

Received: October 25, 2022
Revised: April 18, 2023
Published online: June 28, 2023

[1] J. Železný, P. Wadley, K. Olejník, A. Hoffmann, H. Ohno, *Nat. Phys.* **2018**, *14*, 220.
[2] L. Šmejkal, Y. Mokrousov, B. Yan, A. H. MacDonald, *Nat. Phys.* **2018**, *14*, 242.
[3] B. Dieny, I. L. Prejbeanu, K. Garello, P. Gambardella, P. Freitas, R. Lehndorff, W. Raberg, U. Ebels, S. O. Demokritov, J. Akerman, A. Deac, P. Pirro, C. Adelmann, A. Anane, A. V. Chumak, A. Hirohata, S. Mangin, S. O. Valenzuela, M. C. Onbaşlı, M. d'Aquino, G. Prenat, G. Finocchio, L. Lopez-Diaz, R. Chantrell, O. Chubykalo-Fesenko, P. Bortolotti, *Nat. Electron.* **2020**, *3*, 446.
[4] P. Noel, F. Trier, L. M. Vicente Arche, J. Brehin, D. C. Vaz, V. Garcia, S. Fusil, A. Barthelemy, L. Vila, M. Bibes, J. P. Attane, *Nature* **2020**, *580*, 483.
[5] I. M. Miron, G. Gaudin, S. Auffret, B. Rodmacq, A. Schuhl, S. Pizzini, J. Vogel, P. Gambardella, *Nat. Mater.* **2010**, *9*, 230.
[6] M. D. C., D.-F. Shao, V. D.-H. Hou, P. Quarterman, A. Habiboglu, B. Venuti, M. Miura, B. Kirby, A. Vailionis, C. Bi, X. Li, F. Xue, Y.-L. Huang, Y. Deng, S.-J. Lin, W. Tsai, S. Eley, W. Wang, J. A. Borchers, E. Y. Tsymbal, S. X. Wang, *Nat. Mater.* **2023**, *22*, 591.
[7] L. Liu, C. Zhou, X. Shu, C. Li, T. Zhao, W. Lin, J. Deng, Q. Xie, S. Chen, J. Zhou, R. Guo, H. Wang, J. Yu, S. Shi, P. Yang, S. Pennycook, A. Manchon, J. Chen, *Nat. Nanotechnol.* **2021**, *16*, 277.
[8] D. MacNeill, G. M. Stiehl, M. H. D. Guimaraes, R. A. Buhrman, J. Park, D. C. Ralph, *Nat. Phys.* **2016**, *13*, 300.
[9] N. H. D. Khang, Y. Ueda, P. N. Hai, *Nat. Mater.* **2018**, *17*, 808.
[10] J. Han, A. Richardella, S. A. Siddiqui, J. Finley, N. Samarth, L. Liu, *Phys. Rev. Lett.* **2017**, *119*, 077702.
[11] A. R. Mellnik, J. S. Lee, A. Richardella, J. L. Grab, P. J. Mintun, M. H. Fischer, A. Vaezi, A. Manchon, E. A. Kim, N. Samarth, D. C. Ralph, *Nature* **2014**, *511*, 449.
[12] N. Reynolds, P. Jadaun, J. T. Heron, C. L. Jermain, J. Gibbons, R. Collette, R. A. Buhrman, D. G. Schlom, D. C. Ralph, *Phys. Rev. B* **2017**, *95*, 064412.
[13] L. Liu, C. F. Pai, Y. Li, H. W. Tseng, D. C. Ralph, R. A. Buhrman, *Science* **2012**, *336*, 555.
[14] L. Liu, T. Moriyama, D. C. Ralph, R. A. Buhrman, *Phys. Rev. Lett.* **2011**, *106*, 036601.
[15] J. Sinova, S. O. Valenzuela, J. Wunderlich, C. H. Back, T. Jungwirth, *Rev. Mod. Phys.* **2015**, *87*, 1213.
[16] A. Hoffmann, *IEEE Trans. Magn.* **2013**, *49*, 5172.
[17] H. Chen, Q. Niu, A. H. MacDonald, *Phys. Rev. Lett.* **2014**, *112*, 017205.
[18] Y. Zhang, J. Železný, Y. Sun, J. van den Brink, B. Yan, *New J. Phys.* **2018**, *20*, 073028.
[19] M. Seemann, D. Ködderitzsch, S. Wimmer, H. Ebert, *Phys. Rev. B* **2015**, *92*, 155138.
[20] G. Gurung, D.-F. Shao, E. Y. Tsymbal, *Phys. Rev. B* **2020**, *101*, 140405.
[21] T. Nan, C. X. Quintela, J. Irwin, G. Gurung, D. F. Shao, J. Gibbons, N. Campbell, K. Song, S. Choi, L. Guo, R. D. Johnson, P. Manuel, R. V. Chopdekar, I. Hallsteinsen, T. Tybell, P. J. Ryan, J. Kim, Y. Choi, P. G. Radaelli, D. C. Ralph, E. Y. Tsymbal, M. S. Rzchowski, C. B. Eom, *Nat. Comm.* **2020**, *11*, 4671.
[22] Y. Zhang, Y. Sun, H. Yang, J. Železný, S. P. P. Parkin, C. Felser, B. Yan, *Phys. Rev. B* **2017**, *95*, 075128.
[23] W. Zhang, W. Han, S. H. Yang, Y. Sun, Y. Zhang, B. Yan, S. S. Parkin, *Sci. Adv.* **2016**, *2*, e1600759.
[24] A. Kohn, A. Kovacs, R. Fan, G. J. McIntyre, R. C. Ward, J. P. Goff, *Sci. Rep.* **2013**, *3*, 2412.
[25] K. Kondou, H. Chen, T. Tomita, M. Ikhlas, T. Higo, A. H. MacDonald, S. Nakatsuji, Y. Otani, *Nat. Commun.* **2021**, *12*, 6491.
[26] E. Krén, G. Kádár, L. Pál, J. Sólyom, P. Szabó, T. Tarnóczi, *Phys. Rev.* **1968**, *171*, 574.
[27] E. Krén, G. Kádár, L. Pál, J. Sólyom, P. Szabó, *Phys. Lett.* **1966**, *20*, 331.
[28] Z. Q. Liu, H. Chen, J. M. Wang, J. H. Liu, K. Wang, Z. X. Feng, H. Yan, X. R. Wang, C. B. Jiang, J. M. D. Coey, A. H. MacDonald, *Nat. Electron.* **2018**, *1*, 172.
[29] N. An, M. Tang, S. Hu, H. Yang, W. Fan, S. Zhou, X. Qiu, *Sci. Chin. Phys., Mech. Astron.* **2020**, *63*, 297511.
[30] M. Hayashi, J. Kim, M. Yamanouchi, H. Ohno, *Phys. Rev. B* **2014**, *89*, 144425.
[31] C. O. Avci, K. Garello, M. Gabureac, A. Ghosh, A. Fuhrer, S. F. Alvarado, P. Gambardella, *Phys. Rev. B* **2014**, *90*, 224427.
[32] K. Garello, I. M. Miron, C. O. Avci, F. Freimuth, Y. Mokrousov, S. Blugel, S. Auffret, O. Boulle, G. Gaudin, P. Gambardella, *Nat. Nanotechnol.* **2013**, *8*, 587.
[33] W. Wang, T. Wang, V. P. Amin, Y. Wang, A. Radhakrishnan, A. Davidson, S. R. Allen, T. J. Silva, H. Ohldag, D. Balzar, B. L. Zink, P. M. Haney, J. Q. Xiao, D. G. Cahill, V. O. Lorenz, X. Fan, *Nat. Nanotechnol.* **2019**, *14*, 819.
[34] H. Bai, X. F. Zhou, H. W. Zhang, W. W. Kong, L. Y. Liao, X. Y. Feng, X. Z. Chen, Y. F. You, Y. J. Zhou, L. Han, W. X. Zhu, F. Pan, X. L. Fan, C. Song, *Phys. Rev. B* **2021**, *104*, 104401.
[35] M. H. Nguyen, D. C. Ralph, R. A. Buhrman, *Phys. Rev. Lett.* **2016**, *116*, 126601.
[36] M. R. Fitzsimmons, D. Lederman, M. Cheon, H. Shi, J. Olamit, I. V. Roshchin, I. K. Schuller, *Phys. Rev. B* **2008**, *77*, 224406.

[37] M. G. Kim, H. Miao, B. Gao, S. W. Cheong, C. Mazzoli, A. Barbour, W. Hu, S. B. Wilkins, I. K. Robinson, M. P. M. Dean, V. Kiryukhin, *Nat. Comm.* **2018**, *9*, 5013.
[38] A. A. Sapozhnik, M. Filianina, S. Y. Bodnar, A. Lamirand, M. A. Mawass, Y. Skourski, H. J. Elmers, H. Zabel, M. Kläui, M. Jourdan, *Phys. Rev. B* **2018**, *97*, 134429.
[39] W. Zhang, W. Han, X. Jiang, S.-H. Yang, S. S. P. Parkin, *Nat. Phys.* **2015**, *11*, 496.
[40] Y. Ou, S. Shi, D. C. Ralph, R. A. Buhrman, *Phys. Rev. B* **2016**, *93*, 220405.
[41] X. Chen, S. Shi, G. Shi, X. Fan, C. Song, X. Zhou, H. Bai, L. Liao, Y. Zhou, H. Zhang, A. Li, Y. Chen, X. Han, S. Jiang, Z. Zhu, H. Wu, X. Wang, D. Xue, H. Yang, F. Pan, *Nat. Mater.* **2021**, *20*, 800.
[42] Y. Fan, P. Upadhyaya, X. Kou, M. Lang, S. Takei, Z. Wang, J. Tang, L. He, L. T. Chang, M. Montazeri, G. Yu, W. Jiang, T. Nie, R. N. Schwartz, Y. Tserkovnyak, K. L. Wang, *Nat. Mater.* **2014**, *13*, 699.
[43] B. Maranville, W. Ratcliff Ii, P. Kienzle, *J. Appl. Crys.* **2018**, *51*, 1500.
[44] B. J. Kirby, P. A. Kienzle, B. B. Maranville, N. F. Berk, J. Krycka, F. Heinrich, C. F. Majkrzak, *Curr. Opin. Colloid Interface Sci.* **2012**, *17*, 44.
[45] J. A. Vrugt, C. J. F. ter Braak, C. G. H. Diks, B. A. Robinson, J. M. Hyman, D. Higdon, *Int. J. Nonl. Sci. Num. Sim.* **2009**, *10*, 273.
[46] P. Cueva, R. Hovden, J. A. Mundy, H. L. Xin, D. A. Muller, *Microsc. Microanal.* **2012**, *18*, 667.